Breakup of Liquid Droplets

P. Khare*, D. Ma, X. Chen & V. Yang
Georgia Institute of Technology, Atlanta GA, 30332, USA
Prashant.Khare@gatech.edu and vigor.yang@aerospace.gatech.edu

Abstract

In this paper, deformation and breakup of liquid droplets has been studied. Detailed physics pertaining to four different breakup regimes, oscillatory, bag, multimode and shear breakup, has been investigated using an incompressible interface tracking methodology. Critical Weber numbers for the three regimes have also been indentified for a wide pressure range. A generalized regime diagram valid for $Oh < 0.1$ was developed to predict the breakup mechanism, taking into account the pressure effect on the critical Weber number, using data from previous experimental investigations and simulations conducted during the current study. Child droplet diameters were also characterized during the present research effort and it was concluded that for $We > 300$, the droplet size distribution follows a universal log-normal distribution. A theoretical correlation for sauter mean diameter (SMD), d_{32}, was also developed and it showed decent agreement with the simulation and experimental outcomes.

Introduction

Deformation and breakup of intrinsically unstable liquid droplets resulting from primary atomization, in the presence of a relative fluid velocity, is an important phenomena in a wide range of applications, including, but not limited to, dense spray combustion [1], [2], industrial and agricultural sprays, gas-liquid separators, two-phase flows in chemical reactors, etc. In the particular case of liquid-fueled propulsion systems, such as diesel, gas-turbine and rocket engines, the system performance is conditioned by the fuel and oxidizer droplet size distribution and usually the rate-controlling process in dense sprays [2], [3]. Droplet vaporization, and ensuing combustion, is accelerated if the droplet size is smaller, which makes any process leading to a reduction in drop size, of prime importance in the combustion system design. In dense sprays, mixing of fuel and oxidizer is controlled by the droplet size, which is a direct consequence of the droplet breakup process [1], [4], [5].

Weber number, *We*	$\frac{\rho_g U^2 D}{\sigma}$
Ohnesorge number, *Oh*	$\frac{\mu_l}{\sqrt{\rho_l D \sigma}}$
Reynolds number, *Re*	$\frac{\rho_g U D}{\mu_g}$
Density ratio	$\frac{\rho_l}{\rho_g}$
Viscosity ratio	$\frac{\mu_l}{\mu_g}$
Mach number, *M*	$\frac{U}{a}$

Table 1 Relevant non-dimensional parameters in Newtonian liquid droplet breakup process

Time Scale	Definition	Remarks
Convective time	$\tau_c = D/U$	
Deformation response time	$\tau_r = \sqrt{\frac{\rho_l D^3}{\sigma}}$	$\tau_r^2 = We \frac{\rho_l}{\rho_g} \tau_c^2$
Transport time (gas)	$\tau_{v,g} = \frac{D^2}{\nu_g}$	$\tau_r^2 = \frac{We}{\mathrm{Re}^2} \frac{\rho_l}{\rho_g} \tau_{v,g}^2$
Transport time (liquid)	$\tau_{v,l} = \frac{D^2}{\nu_l}$	$\tau_r^2 = \frac{We}{\mathrm{Re}^2} \frac{\rho_l}{\rho_g} \frac{\nu_l^2}{\nu_g^2} \tau_{v,l}^2$

Table 2 Time Scales

Several reviews on droplet deformation and breakup were conducted in the pas [1], [2], [4], [6], [7], [8], [9], [10]. Various non-dimensional parameters dictating the droplet deformation and breakup phenomena were identified as listed in Table 1. Here, D is the diameter of the droplet; U, the relative velocity of the droplet with respect to the ambient; ρ_g and ρ_l, the density of the liquid and gaseous phases; μ_g and μ_l, the gas and liquid viscosities; a is the

*Corresponding author: Prashant.Khare@gatech.edu

speed of sound and σ is the surface tension of the liquid phase. Based on the Weber number, droplet breakup has been classified into breakup modes [6], [9], [11], [12], [13]. The various breakup regimes identified by Hsiang and Faeth [12], at atmospheric pressure for a wide variety of fluids are shown in Figure 1 for $\rho_l/\rho_g > 500$. The breakup of droplets can be broadly categorized into oscillatory, bag, multimode, shear and piercing regimes with respective critical Weber numbers shown in the figure. Interestingly, the figure shows that Ohnesorge number does not have a significant effect on the breakup mechanism for *Oh* < 0.1. Figure 1 also shows the variation of Ohnesorge number as the droplet diameter changes for various fluids. The black square symbol shows *Oh* = 0.1, corresponding to a water droplet of diameter 0.85 μm, which is smaller than droplet sizes for most practical purposes. By definition, Ohnesorge number decreases with increasing droplet diameter, hence the operating region in this paper is *Oh* < 0.1, as shown by the shaded portion of Figure 1. As a result, for the current study, the most important non-dimensional dictating droplet breakup physics is the Weber number.

As a droplet moves though an environment with a velocity relative to the ambient, it is acted upon by aerodynamic drag force. The drag force, in turn, creates differential pressure distribution around the droplet causing it to deform. The other forces acting on the droplet are the internal and external skin friction force due to the droplet and gas viscosity. The inertial, surface tension and viscous forces acting on the droplet can be associated with multiple time and length scales governing the droplet breakup phenomena. Table 2 shows the various time scales of interest. The convective time scale, τ_c, is dictated by the droplet initial diameter and velocity, irrespective of the fluid, and represents the time which the droplet spends in the region of interest. A more non-intuitive and interesting time scale is the deformation response time, τ_r, which is dependent on the physical properties of the droplet. It can be defined at the time required for the droplet to assemble its "resources" to resist the change in shape due to externally imposed forces. For example, if the droplet is made of a non-deformable substance, i.e., $\sigma \to \infty$, $\tau_r \to 0$, which means that the droplet instantaneously responds to the external force, that it will not undergo deformation. On the other hand if a liquid droplet is at supercritical conditions, where $\sigma \to 0$, $\tau_r \to \infty$, suggesting that the droplet will never respond to a force trying to deform it because no resisting force is present. The transport or the viscous time scale, $\tau_{v,l}/\tau_{v,g}$, represents the time required for the viscous forces to come into effect during the whole process. The length scales includes, the various curvatures formed during the deformation process, as well the myriads of different sized ligaments and child droplets produced during, and after the breakup process. The presence of disparate length and time scales, along with the complex physics, makes this a formidable problem, theoretically, experimentally and computationally.

As stated before, depending on the magnitude of the inertial force as compared to the restoring surface tension force, the droplet breaks up via oscillatory, bag, multimode or shear breakup mechanism. Figure 2 shows the schematic of the various breakup modes observed by researchers for Newtonian droplets exposed to subsonic and supersonic air streams [3], [11], [14], [15], [16], [17], [18], [19], as well as the forces acting on the droplet. A few studies on highly viscous and non-Newtonian droplet breakup under the action of an air jet have also been reported [14], [15], [20], [21], [22]. In addition to experiments listed before, shock tube experiments have also been conducted to study the breakup characteristics of single droplets due to the flow behind the disturbance created by a travelling shock wave [4], [12], [13], [19], [20], [23], [24], [25], [26], [27], [28], [29].

In contrast to experimental studies, limited efforts have been applied to simulate and model the droplet breakup phenomena. Han and Tryggvason [30], [31] conducted numerical investigations to study the effect of constant force and impulsive acceleration on droplet deformation, using a compressible, axisymmetric interface tracking technique. The work was limited to small density ratios of 1.15 and 10 and did not consider droplet breakup. The same problem was later simulated by Quan and Schmidt [32] to examine the deformation and droplet drag using an incompressible, finite volume staggered mesh method coupled with a moving mesh interface tracing scheme. Khosla et al. [33] conducted 3D and axisymmetric calculations using the volume-of-fluid (VOF) approach to study the breakup of a single liquid drop by gas crossflow.

The present work is aimed at investigating detailed flow and structure dynamics of liquid droplet breakup. The purpose is to establish high-fidelity modeling techniques to explore the detailed flow evolution during droplet deformation and breakup, and to extract essential physics dictating the flow characteristics. As pointed before, since limited literature exists for droplet breakup at low density ratios, during the present research, emphasis has been placed on droplet deformation and breakup at elevated pressures, which also represents typical pressure conditions in a rocket combustion chamber. To isolate the hydrodynamic mechanisms dictating droplet breakup phenomena, evaporation is neglected, and simulations are performed at isothermal conditions. The phenomenology for various breakup modes is identified based on the temporal evolution of shape, flow field, and energies associated with the deforming and breaking droplet. Finally, a generalized regime diagram, based on the critical Weber number at

elevated pressures, obtained from the present simulations, and previous experimental data at atmospheric conditions, is constructed, valid for *Oh* < 0.1. Droplet size distribution is studied next to complete the study.

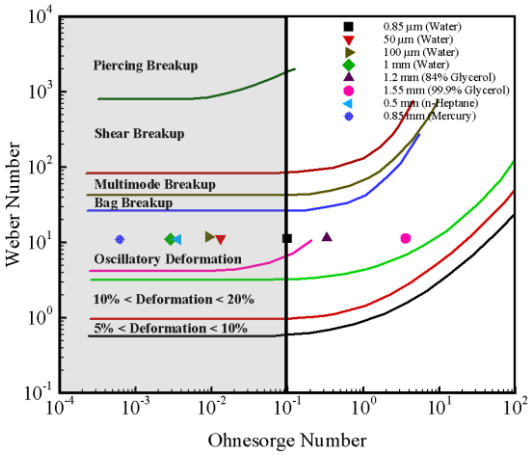

Figure 1 Breakup regime diagram, 1 atm. Variation of *Oh* for a fixed *We = 11* with change in diameter.

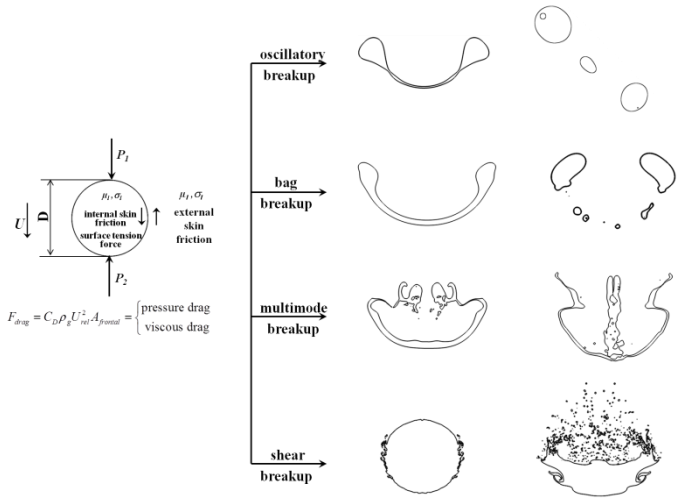

Figure 2 Various droplet breakup patterns.

Theoretical and Numerical Framework

The theoretical formulation of this multi-phase, multi-fluid problem, is based on a three-dimensional, incompressible, variable-density, conservation equations with surface tension [34] and can be written as

$$\frac{\partial \rho}{\partial t} + \nabla.(\rho \vec{u}) = 0 \qquad (1)$$

$$\rho\left(\frac{\partial \vec{u}}{\partial t} + \vec{u}.\nabla\vec{u}\right) = -\nabla p + \nabla.(2\mu\overline{\overline{D}}) + \sigma\kappa\delta_s n \qquad (2)$$

where $\vec{u} = (u, v, w)$ is the fluid velocity, $\rho = \rho(\vec{x}, t)$ the density, $\mu = \mu(\vec{x}, t)$ the dynamic viscosity, and $\overline{\overline{D}}$ the deformation tensor defined as $D_{ij} = \frac{1}{2}\left(\frac{\partial u_i}{\partial x_j} + \frac{\partial u_j}{\partial x_i}\right)$. The Dirac delta distribution function δ_s expresses the fact that the surface tension term is concentrated on the interface. σ is the surface tension coefficient and κ and n the radius of curvature and the unit vector normal to the interface, respectively.

A volume-of-fluid (VOF) variable $c = c(\vec{x}, t)$ is introduced to trace the multi-fluid interface. It is defined as the volume fraction of a given fluid in each computational cell. The density and viscosity can be defined as

$$\rho(c) = c\rho_1 + (1-c)\rho_2 \qquad (3)$$

$$\mu(c) = c\mu_1 + (1-c)\mu_2 \qquad (4)$$

The subscripts 1 and 2 denote the first and second fluid, respectively. According to mass continuity, the advection equation for the density can then be written as an equivalent equation for the volume fraction, given by

$$\frac{\partial c}{\partial t} + \nabla.(c\vec{u}) = 0 \qquad (5)$$

The theoretical formulation outlined above is solved numerically using a finite volume method augmented by an adaptive mesh refinement (AMR) technique to improve the solution accuracy and efficiency. It is clearly seen that grid adapts to capture the interface of the droplet. The above mentioned approach has been successfully applied and validated by several researchers in the past [34], [35], [36], [37], [38], [39], [40].

Results and Discussion

Oscillatory Breakup

This is the least violent of all the breakup modes. If a 100 µm water droplet is given an initial velocity of 12 m/s to achieve a *We* = 24, *Re* = 7609, at a density ratio of $\rho_l/\rho_g = 8.29$, oscillatory breakup is observed. Figure 3 shows the temporal evolution of events taking place during the oscillatory breakup of a droplet. The flowfield is first

plotted in drop coordinate system as shown in Figure 4 a, b, c and d. As the droplet starts moving in the quiescent ambient, it creates two counter rotating vortices. Static pressure at the forward and rear stagnation points is higher than that at the sides, which is typical for flow over a sphere. This unequal static pressure distribution causes the droplet to deform laterally to form an ellipsoid shape. As the droplet deforms further, it forms a bowl as shown in Figure 4c due to higher pressure within the bowl. The oscillation further leads to the formation of a dome followed by the stretching of the droplet in the flow direction, after which, it eventually breaks, first from the bottom, and then from the top, giving birth to two child and a satellite droplet. The breakup takes place via pinch-off, as result of shear stresses created by the surface tension force which tries to minimize the surface area causing the liquid interface to recede and creating concentrated shear stresses. As the droplet deforms, the velocity at different points inside the droplet is different and hence it becomes impossible to plot the results in a coordinate system fixed to the droplet, and so from here onwards, the results will be presented in fixed coordinate system as shown in Figure 4e and Figure 4f.

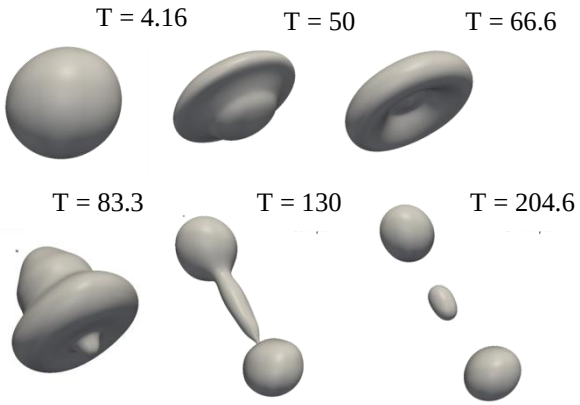

Figure 3 Oscillatory breakup - *We* = 24, *Re* = 7609, $\rho_l / \rho_g = 8.29$; T: time in µs.

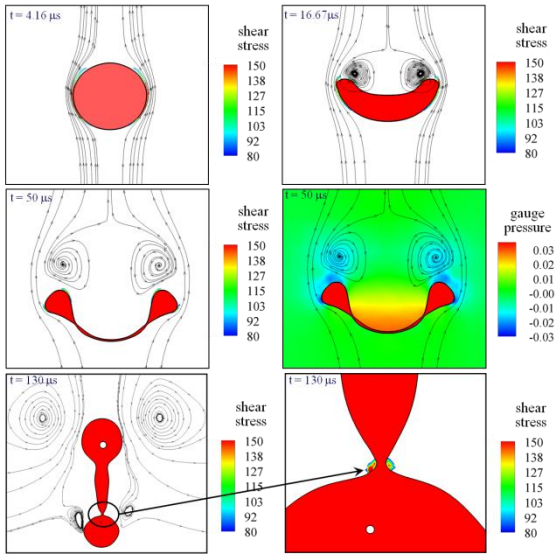

Figure 4 Evolution of flow field around the droplet for oscillatory breakup mode.

Bag and Multimode Breakup

As the Weber number is increased beyond ~30, the breakup mechanism changes. Temporal events taking place when a 50 µm water droplet is subjected to an initial velocity of 20 m/s are shown in Figure 5. This corresponds to a *We* = 33, *Re* = 6342 at a density ratio, $\rho_l / \rho_g = 8.29$. As in the case of oscillatory breakup, the droplet deforms due to unequal pressure distribution over the droplet periphery into an elliptic disc. This is followed by the formation of a thin bag/balloon. It should be noted that we see the formation of a bowl rather than a dome shape because of higher Reynolds number and is consistent with the observations and correlations presented by Hsiang & Faeth [12]. The breakup mechanism is still bag because of the higher ambient pressure and has phenomenological resemblance to the axisymmetric simulations conducted by Han & Tryggvason [31] at lower density ratios when the droplet was subjected to an impulsive acceleration. The formation and thinning of the bag is due to the higher pressure inside the bag as shown in Figure 6. As the droplet moves further into the ambient, the higher pressure within the bag causes the liquid to move towards the rim making it thicker than the bag. The bag, which is progressively becoming thinner, eventually cracks at multiple locations to form a web like structure, which propagates further and breaks up the bag into smaller ligaments and child droplets. The breaking of the bag is caused due to the breakup of the thin bag, which essentially behaves as thin sheet, by capillary instability as shown in the zoomed in picture at the bottom right of Figure 6. This event is followed by the breakup of the rim to form another set of child droplets.

Figure 7 shows the multimode breakup regime. This breakup phenomenology was observed when a 100 µm water droplet was given and initial velocity of 42 m/s to achieve a *We* = 292. Typical temporal evolution of droplet deformation and breakup in the multimode breakup regime is shown in the figure. As clearly seen, the droplet morphology during the breakup process is similar to bag breakup with an additional stem oriented in the direction opposite to the droplet motion. The events leading to the formation of the bag are similar to that of the bag breakup

regime except for the fact that due to a higher inertial force, the droplet rim gets thinner forming a "lip". In other words, the time scale governing the motion of the liquid from the bottom to the top of the droplet is much larger than the "effective" time scale associated with the action of inertial forces on the droplet. This also leads to the formation of a stem which protrudes from the bottom of the droplet. Once the droplet slows down due to aerodynamic drag, a rim and a bag is formed, similar to the bag breakup regime. Meanwhile, the lip along with the bag stretches and undergoes thinning. The formation of the lip causes a recirculation zone and creates a low pressure region inside the droplet, just below the rim. This difference in pressure leads to lip thinning, eventually leading to its breakup, followed by the breakup of bag, rim, and the stamen. Depending on the flow conditions, the initial breakup can take place in the bag or the lip.

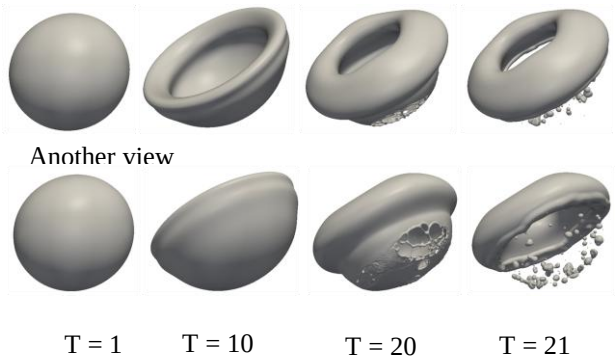

Figure 5 Bag breakup - *We* = 33, *Re* = 6342, $\rho_l / \rho_g = 8.29$; T: time in µs.

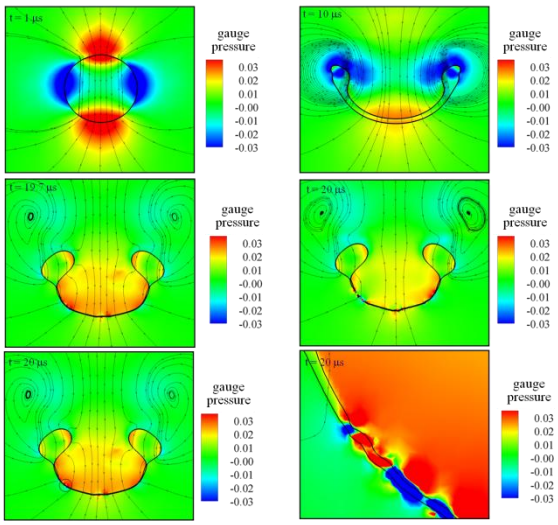

Figure 6 Normalized gauge pressure distribution in the droplet periphery at 1, 10, 19.7 and 20 µs.

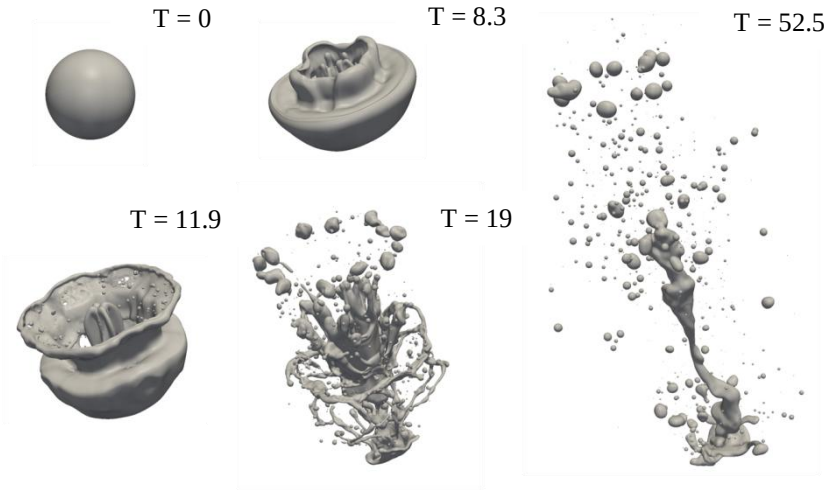

Figure 7 Multimode breakup - *We* = 292, *Re* = 26635, $\rho_l / \rho_g = 8.29$; T: time in µs.

Shear Breakup

As shown in Figure 8, shear breakup is the most violent of the four breakup regimes discussed in this paper. In this particular case, the Weber number is 4237 at a density ratio of $\rho_l / \rho_g = 8.29$. The time required for shear breakup is the lowest in comparison to the other three regimes. Shear thinning of the droplet from the periphery leads to the breakup of the droplet in this case, which is consistent with the observations made by several researchers in the past [21], [33], [41], [42], [43], [44]. The aerodynamic force exerted by the surrounding fluid causes deflection and thinning of the droplet periphery owing to Rayleigh-Taylor instability. The film then breaks up into

ligaments and child droplets. Capillary instability causes the breakup of ligaments to form the final droplet distribution.

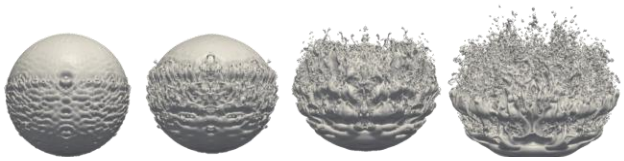

T = 0.5 T = 1 T = 2 T = 3.2

Figure 8 Shear breakup - *We* = 4327, *Re* =162350, $\rho_l / \rho_g = 8.29$; T: time in μs.

Generalized Regime Diagram

A thorough parametric study was conducted to identify the critical Weber number for the various breakup modes discussed in this paper. It is quite clear from the above results that the critical Weber number corresponding to different breakup regimes are dependent on the density ratio, which can be regarded as a manifestation of pressure, along with the more important Weber number. The critical Weber numbers at lower density ratio are much different as compared to the one's found in the literature for higher density ratios, or equivalent lower pressure conditions [12], even though the experimental data consisted of quite a wide range of density ratios. It should be pointed out that, the density ratio, in the experiments was varied by changing the liquid as opposed to changing the ambient density, which was the case in the present numerical study. The differences, observed in critical Weber numbers at elevated pressure conditions can be explained using the fact that at higher pressures, the drag experienced by the droplet is much higher. This means that the rate of change of momentum is much higher at lower density ratios conditions created by high pressures. This reduction in relative velocity, reduces the instantaneous relative velocity and hence a higher Weber number is required by the droplet to undergo deformation and breakup at higher pressure conditions. A model was developed to take into account the pressure effect on the critical Weber number as show below in equation 6, for *Oh* < 0.1. It can be clearly seen that, as $p \to p_{cr}$, $We_{cr,p} \to \infty$, since $\sigma \to 0$ as $p \to p_{cr}$.

$$We_{cr} = We_{cr,ref}\left\{1+\frac{c}{1-p_r}We_{cr,ref}\left[\left(\frac{\rho_g}{\rho_l}\right)-\left(\frac{\rho_g}{\rho_l}\right)_{ref}\right]\right\},\ p_r=\frac{p}{p_{cr}},\ p_{ref}=1\text{ atm},\ c=0.62 \tag{6}$$

Figure 9 shows the generalized regime diagram based on the developed model. The black, green, red and blue symbols represent the critical Weber numbers for bag, multimode and shear breakup regimes at 1, 25, 60 and 100 atm pressures, respectively.

Child Droplet Diameter Distribution

Child droplet diameters were studied for a wide range of Weber numbers. Interestingly, it was found that the probability density distribution of the droplet diameters, shifted by a probability of 0.05, could be correlated using a log-normal distribution for *We* > 300 given by:

$$pdf = \frac{1}{d\sigma\sqrt{2\pi}}\exp\left\{-\frac{\left(\ln(d)-\mu\right)^2}{2\sigma^2}\right\} \quad \text{for} \quad We > 300 \tag{7}$$

where d is the representative child droplet diameter, μ and σ are the correlation constants. It is found that the PDFs are decidedly similar with almost the same μ and σ as listed in Table 3.

The end of breakup marked is marked by the equilibrium of surface tension and inertial aerodynamic forces. If an effective representative sphere of diameter, d, is assumed for a given volume of liquid, the surface tension and aerodynamic forces can be written as:

$$F_{aerodynamic} = \frac{1}{2}C_d\rho_g u_{rel}^2 A_{frontal},\ where\ A_{frontal} = \frac{\pi d^2}{4} \tag{8}$$

$$F_{surf.tension} = \sigma\pi d \tag{9}$$

$$\text{At equilibrium, } F_{aerodynamic} = kF_{surf.tension}$$

$$d = \frac{8k\sigma}{C_d\rho_g u_{rel}^2} \Rightarrow \frac{d}{D} = \frac{8k}{C_d We} \tag{10}$$

The sauter mean diameter (SMD), d_{32}, was calculated from the present DNS calculations. It can be correlated using the above analysis by assuming that d_{32} is proportional to d, given by:

$$\frac{d_{32}}{D} = kf(We)\frac{d}{D} \tag{11}$$

where *f(We)* is chosen not only because it is the most important non-dimensional quantity in the present physical situation but also since it represents a quantity similar to d_{32}. Figure 10 shows the predicted SMD along with the one obtained from the simulation. *f(We)* is given by:

$$kf(We) = We^{0.28} \tag{12}$$

Excellent agreement between the model and the numerical data is observed. The results for SMD for shear breakup regime, which we define beyond Weber numbers of approximately 1000 for 100 atm pressure conditions, seems to asymptote to a value near 0.1, which agrees well with the quasi steady correlation developed by Chou, et al. [24] where they propose SMD/D = 0.09 (with a 22% standard deviation) for the shear breakup regime. If we use our generalized correlation to obtain the corresponding Weber number at 100 atm which pertains to the same breakup physics as exhibited by Weber number of 125 for water/air system at 1 atm, and used equation 11, we find that our SMD correlation yields a value of 0.11, which is quite close to the experimental predictions and lies with the range of experimental error. This further validates the used approach and the generalized regime diagram developed during the course of this study.

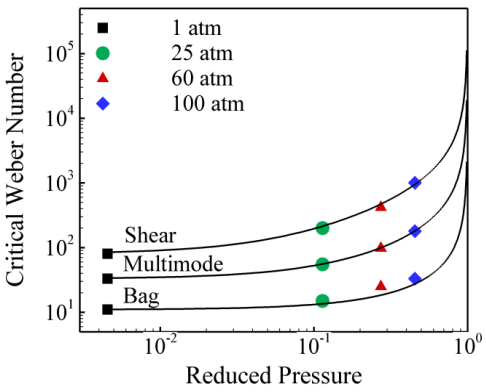

Figure 9 Generalized regime diagram.

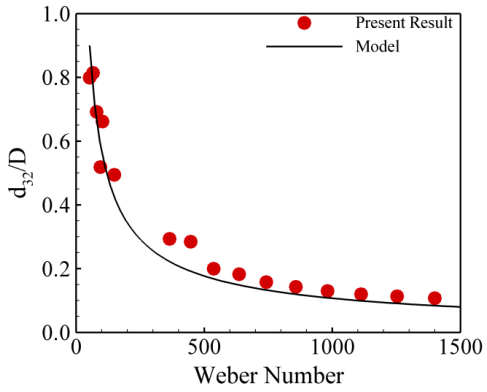

Figure 10 Sauter mean diameter, d_{32}, correlated using an analytical model.

Weber number	μ	σ
365	0.2395	0.4010
447	0.2417	0.3646
537	0.2357	0.3753
636	0.2384	0.4005
742	0.2626	0.3877
981	0.248	0.4041
1112	0.2879	0.4120
1253	0.3182	0.4218
1400	0.2926	0.3947

Table 3 Correlation coefficients μ and σ for a range of Weber numbers

Conclusions

Various mechanisms leading to the deformation and breakup of Newtonian droplets at varying pressures have been explored in this paper using an AMR enhanced, incompressible VOF methodology. Four different mechanisms, namely, oscillatory, bag, multimode, and shear breakup modes were studied. Weber number governs the transition from one breakup mechanisms to another. Child droplet diameter correlations were also developed and it was found that a log-normal distribution fits the child droplet diameter distribution. The distribution seemed to be similar for Weber number greater than about 300. For smaller Weber numbers, the distribution was found to be discontinuous due to smaller inertial force associated with it. An analytical model was also developed to predict the SMD of droplet distribution which agrees well with simulation and experimental data. Another highlight of the

current work was the development of a generalized regime diagram, which was based on the current simulation results, along with data obtained from the literature to predict the critical Weber numbers at a wide range of pressure conditions.

Acknowledgements

This work was sponsored by the US Army Research Office under the Multi-University Research Initiative (MURI) under contract number W911NF-08-1-0124. The support and encouragement provided by Dr. Ralph Anthenien is greatly acknowledged. The authors are also thankful to Dr. Stephane Popinet for allowing them to use his VOF and AMR algorithms.

References

[1] Faeth, G.M., *Twenty-Sixth Symposium (International) on Combustion. The Combustion Institute* 26 1593-1612 (1996).
[2] Faeth, G.M., ILASS-Europe, Zaragoza, Spain, 2002.
[3] Berthoumieu, P., Carentz, H., Villedieu, P. and Lavergne, G., *International Journal of Heat and Fluid Flow* 20 492-498 (1999).
[4] Faeth, G.M., Hsiang, L.P. and Wu, P.K., *International Journal of Multiphase Flow* 21 99-127 (1995).
[5] Ruff, G.A., Wu, P.K., Bernal, L.P. and Faeth, G.M., *J Propul Power* 8 280-289 (1992).
[6] Pilch, M. and Erdman, C.A., *International Journal of Multiphase Flow* 13 741-757 (1987).
[7] Guildenbecher, D.R., Lopez-Rivera, C. and Sojka, P.E., *Experiments in Fluids* 46 371-402 (2009).
[8] Wierzba, A. and Takayama, K., *Aiaa J* 26 1329-1335 (1988).
[9] Hinze, J.O., *AIChE Journal* 1 289-295 (1955).
[10] Gefland, B.E., *Prog Energ Combust* 22 201-265 (1996).
[11] Krzeczkowski, S.A., *International Journal of Multiphase Flow* 6 227-239 (1980).
[12] Hsiang, L.P. and Faeth, G.M., *International Journal of Multiphase Flow* 21 545-560 (1995).
[13] Hsiang, L.P. and Faeth, G.M., *International Journal of Multiphase Flow* 18 635-652 (1992).
[14] Arcoumanis, C., Khezzar, L., Whitelaw, D.S. and Warren, B.C.H., *Experiments in Fluids* 17 405-414 (1994).
[15] Arcoumanis, C., Whitelaw, D.S. and Whitelaw, J.H., *Atomization and Sprays* 6 245-256 (1996).
[16] Miller, B., Sallam, K.A., Bingabr, M., Lin, K.C. and Carter, C., 45th AIAA Aerospace Sciences Meeting, AIAA, Reno, NV, 2007, pp. 15993-16004.
[17] Theofanous, T.G., Li, G.J. and Dinh, T.N., *Journal of Fluids Engineering* 126 516-527 (2004).
[18] Borisov, A.A., Gel'fand, B.E., Natanzon, M.S. and Kossov, O.M., *Journal of Engineering Physics and Thermophysics* 40 44-49 (1981).
[19] Gel'fand, B.E., Gubin, S.A. and Kogarko, S.M., *Journal of Engineering Physics and Thermophysics* 27 119-126 (1974).
[20] Joseph, D.D., Belanger, J. and Beavers, G.S., *International Journal of Multiphase Flow* 25 1263-1303 (1999).
[21] López-Rivera, C. and Sojka, P., ICLASS 2009, 11th Triennial International Annual conference on Liquid Atomization and Spray Systems, Vail, Colorado, 2009.
[22] López-Rivera, C., Mechanical Engineering Department, Purdue University, 2010, pp. 170.
[23] Hsiang, L.P. and Faeth, G.M., *International Journal of Multiphase Flow* 19 721-735 (1993).
[24] Chou, W.H., Hsiang, L.P. and Faeth, G.M., *International Journal of Multiphase Flow* 23 651-669 (1997).
[25] Chou, W.H. and Faeth, G.M., *International Journal of Multiphase Flow* 24 889-912 (1998).
[26] Dai, Z. and Faeth, G.M., *International Journal of Multiphase Flow* 27 217-236 (2001).
[27] Ranger, A.A. and Nicholls, J.A., AIAA 6th Aerospace Sciences Meeting, AIAA, New York, NY, 1968.
[28] Krauss, W.E. and Leadon, B.M., AIAA Aerospace Sciences Meeting, AIAA, 1971.
[29] Boiko, V.M., Papyrin, A.N. and Poplavskii, S.V., *Journal of Applied Mechanics and Technical Physics* 28 263-269 (1987).
[30] Han, J. and Tryggvason, G., *Phys Fluids* 11 3650-3667 (1999).
[31] Han, J. and Tryggvason, G., *Phys Fluids* 13 1554-1565 (2001).
[32] Quan, S. and Schmidt, D.P., *Phys Fluids* 18 102103-102109 (2006).
[33] Khosla, S., Smith, C.E. and Throckmorton, R.P., ILASS Americas, 19th Annual Conference on Liquid Atomization and Spray Systems, Toronto, Canada, 2006.
[34] Pópinet, S., *J Comput Phys* 228 5838-5866 (2009).
[35] Pópinet, S. and Rickard, G., *Ocean Modelling* 16 224-249 (2006).
[36] Tomar, G., Fuster, D., Zaleski, S. and Popinet, S., *Computers and Fluids* 39 1864-1874 (2010).
[37] Ma, D., Chen, X., Khare, P. and Yang, V., 49th AIAA Aerospace Sciences Meeting, AIAA, Orlando, FL, 2011.
[38] Chen, X., Ma, D., Khare, P. and Yang, V., 49th AIAA Aerospace Sciences Meeting, AIAA, Orlando, FL, 2011.
[39] Chen, X., Ma, D., Khare, P. and Yang, V., 7th US National Technical Meeting of the Combustion Institute, Atlanta, GA, 2011.
[40] Khare, P., Ma, D., Chen, X. and Yang, V., 50th AIAA Aerospace Sciences Meeting, Nashville, TN, 2012.
[41] Lee, C.H. and Reitz, R.D., *Atomization and Sprays* 9 497-517 (1999).
[42] Lee, C.H. and Reitz, R.D., *International Journal of Multiphase Flow* 26 229-244 (2000).
[43] Lee, C.S. and Reitz, R.D., *Atomization and Sprays* 11 1-19 (2001).
[44] Liu, Z. and Reitz, R.D., *International Journal of Multiphase Flow* 23 631-650 (1997).